Hindawi
Shock and Vibration
Volume 2019, Article ID 5814172, 11 pages
https://doi.org/10.1155/2019/5814172

Research Article

Experimental Study of Blast Resistance on BFRP Bar-Reinforced Cellular Concrete Slabs Fabricated with Millimeter-Sized Saturated SAP

Jun-ru Ren, Hua Cheng, Chao-shan Yang, and Rui-xi Dai

Department of Military Installations, Army Logistical University of PLA, Chongqing 401311, China

Correspondence should be addressed to Jun-ru Ren; renjunru81@foxmail.com

Received 23 July 2019; Revised 11 September 2019; Accepted 23 September 2019; Published 14 October 2019

Academic Editor: Mario Terzo

An innovative cellular concrete procured with sat-SAP (superabsorbent polymer) is introduced. Combined with BFRP bars, this concrete may play a role as protective structures in marine applications. Eight BFRP-reinforced cellular concrete slabs (BSs) and three steel-reinforced normal concrete slabs (SPs) are exposed to simulated blast loadings in a shock tube device. Low-modulus cellular concrete and BFRP bars cause BSs to exhibit distinctive behaviours compared to those of SPs. BSs, which are more flexible at the same reinforcement ratio, have more intensive vibrations and larger deformations compared to SPs under various blast loadings. In addition to the porous structure of cellular concrete, BSs demonstrate better wave-attenuating and energy-absorbing abilities. More severe damage such as cracks, deflections, and breaches is observed for BSs. In the current research, a comprehensively superior blast resistance can be achieved through improving reinforcement ratio to promote serviceability.

1. Introduction

The constantly evolving threat of terrorism remains one of the greatest challenges to global security. As terrorist bombing attacks have raged higher, especially after the collapse of the World Trade Center in the 9/11 attacks, concerns about the blast resistance of buildings and other socioeconomically critical structures have increased. In construction, steel-reinforced concrete is undoubtedly the most widely used building material, while in some special fields, such as offshore engineering and reef engineering, this concrete might lack durability and economy. Hence, it is crucial to understand the response of structures and to develop novel materials and techniques to improve the blast resistance of buildings.

The addition of superabsorbent polymers (SAPs) in concrete to ease self-desiccation and shrinkage is common [1, 2]. Unlike the most used SAPs with a diameter less than 500 μm, Cheng et al. [3] pioneered the use of spherical saturated SAPs with a diameter of 5–7 mm as a full or partial substitute for the coarse aggregates in traditional concrete and consequently fabricated a novel cellular concrete. Dry SAPs were polyacrylic acid-based particles with a diameter of 1.5–2 mm and a density of 1360 kg/m^3. Owing to the small size and lightweight, the cellular structure could definitely reduce the dead load and transportation work of raw materials for the construction of remote islands. Deng et al. [1] elaborated the manufacturing process, as shown in Figure 1. With the gradual dehydration and shrinkage of saturated SAP beads in the curing process, evenly distributed millimeter-sized pores were achieved in the cellular concrete. A low Young's modulus and pores have also been verified to bring advantages to protective engineering [4, 5]. Under SHPB experiments [1] and simulations [6], the compressive strength and elastic modulus of cellular concrete were evidently strain rate dependent, which was related to the porosity and paste strength. The hindering effect of the pores on the velocity of the stress wave induced a decline of DIF-E with porosity. In addition, the porous structure could effectively attenuate stress waves, especially in high-porosity specimens, and the attenuation effect was positively proportional to the pulse time of the stress wave. A significant

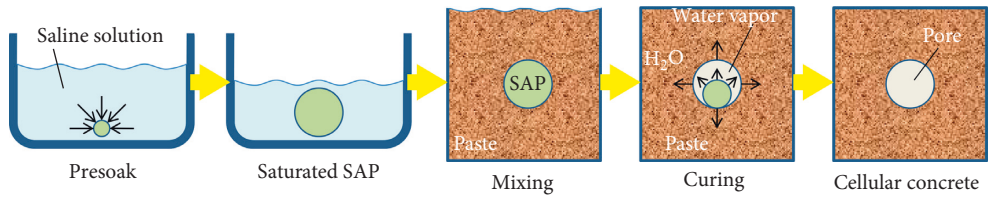

Figure 1: A schematic of the fabrication process of cellular concrete (arrows represent the flow direction of water and vapor) [1].

dispersion of stress waves combined with constitutive dispersion and interface diffusion was likewise detected.

FRP bars are now the most promising alternative to steel bars in construction and have recently attracted the attention of the scientific community. The high strength, lightweight, and excellent acid and alkali resistance properties of FRP bars provide great potential for marine construction [7, 8], especially for reef construction far from the mainland to reduce traffic and maintenance expenses. Some researchers [9–11] have attempted to incorporate FRP bars in the abovementioned cellular concrete to fabricate structural components such as beams and columns. Zhu et al. [9] presented an empirical model for the bond behaviour between FRP bars and cellular concrete. Although the porous structure affected the bond-slip properties, these materials could work well together similar to normal steel rebar concrete. Zheng et al. [10] proposed numerical methods to design beam components with FRP bars and cellular concrete. Both materials acquired a lower elastic modulus than conventional steel reinforcement and concrete, and the composite just deforms compatibly and obtains larger deflections. Gu and Wang [11] carried out the static experiment on twelve carbon-glass FRP bar-reinforced cellular concrete columns with various reinforcement ratios, slenderness ratios, and stirrup space. Under uniaxial static loading, most columns failed because of the crushing of concrete with intact bars.

Basalt fibres, obtained from volcanic rock through melting (1300–1700°C) and spinning into fine fibres, were prominently less expensive than other fibres and were characterized by very engaging physical and chemical properties, such as a high strength and temperature and a good anticorrosion ability, long-term durability, and good processability [12]. Similar to other fibre materials, basalt fibres integrated with a resin matrix were also employed in innovative structures for strengthening or retrofitting. In most studies of FRP bar-reinforced concrete structures, attention has been given to the static properties [13–16]. Mahroug et al. [13] compared the test results and design codes through experiments on six slabs reinforced with BFRP bars and found that the compounded shear-deflection failure led to a lower failure moment than the codes estimated. In addition, the bond durability in aggressive environments [14], the corrosion resistance, and the mechanical behaviour of structural components reinforced with BFRP rods [13, 15, 16] have been analysed and reported by other investigators.

To the best of our knowledge, only Feng et al. [17] placed BFRP-reinforced concrete slabs to close-in explosion to study their blast resistance performance. The results demonstrated that concrete members made with high-strength and low-stiffness BFRP bars exhibited large deformation and a great load capacity because of the long elastic deformation of the BFRP bars. With damage modes of cracks, spalls, and breaches, BFRP bar-reinforced slabs had a better antidetonation ability compared to steel bar-reinforced concrete slabs in some blast cases. Through combining the BFRP bar and cellular concrete, a major thrust of this paper is to investigate its dynamic response through shock tube experiments to explore further possible marine application.

2. Experimental Work

2.1. Slabs. As presented in Figure 2 and Table 1, nine BFRP bar-reinforced cellular concrete slabs (BSs) and three steel rebar-reinforced normal concrete slabs (SPs) were fabricated in the experiment. The dimensions of all slab specimens were 500 mm × 300 mm × 40 mm. The reinforcements have the same diameter of 6 mm with only one layer in the middle of the specimens. According to ACI440.1R-06 [18], the spacing of lateral BFRP bars in the BSs was 65 mm, 90 mm, and 150 mm, indicating ratios of 0.5%, 0.8%, and 1.1%, respectively. The SPs adopted one reinforcement ratio of 0.8%.

2.2. Materials. Commercially available ordinary Portland cement (OPC) of Grade 52.5 and sulphoaluminate cement (SAC) of Grade 42.5 were used. General-purpose silicon fume (SF) with a specific surface area of 25000 m^2/kg and an SiO_2 content of 95% was also utilized to fill the voids and strengthen the mortar matrix. Class F fly ash with 2000 mesh (low calcium) was added to the mixture. Fine aggregates (RS) and coarse aggregates (G) in the SSD condition were employed. The coarse aggregates (G) were crushed limestone from a local quarry with a size of 5–25 mm, and the fine aggregates were river sand with a fineness modulus of 2.58. A liquid polycarboxylic acid superplasticizer (PS) was dissolved in mixing water to adjust the workability of the mixture. Polypropylene (PP) fibres of 9 mm–3 mm and with a diameter of 31 μm were applied to mitigate SAP rising and crack. The mixing water (W) was a sodium chloride (NaCl) solution with a concentration of 1 mol/L and normal tap water for the cellular concrete and the conventional concrete, respectively. Dry SAP was soaked in the same NaCl solution for at least 8 h in advance. The SAP gained a maximum water absorptivity of 14.2 [2, 3] and became spherical with a diameter of 5–7 mm.

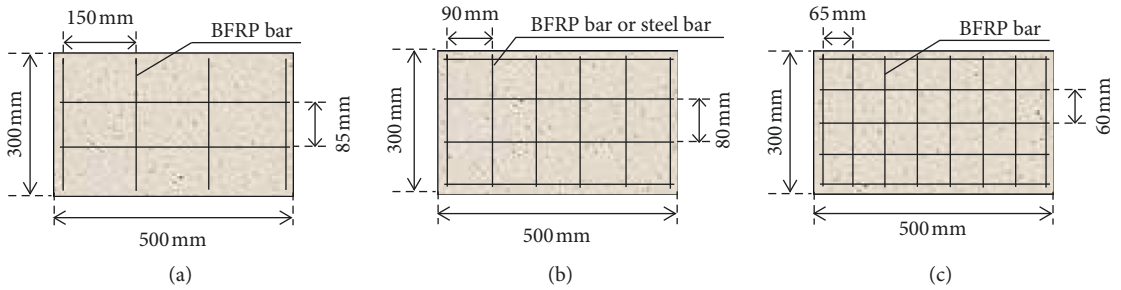

Figure 2: Configuration of specimens.

Table 1: Specimens for the experiment.

Specimen ID	Inflation pressure (MPa)	Reinforcement ratio		
		0.5%	0.8%	1.1%
Steel rebar-reinforced normal concrete (SP)	4.5		SP2-1	
	5.5		SP2-2	
	6.5		SP2-2	
BFRP bar-reinforced cellular concrete (BS)	4.5	BS1-1	BS2-1	BS3-1
	5.5	BS1-2	BS2-2	BS3-2
	6.5	BS1-3	BS2-3	BS3-3

2.3. Concrete Preparation. The mixture proportions of the cellular concrete and the normal concrete are provided in Tables 2 and 3. Given the low density of the saturated SAP, which is close to 1, it can possibly float in mortar during mixing and curing. To obtain the cellular concrete with uniformly distributed sat-SAP beads, measurements were taken in the mixture design. Sulphoaluminate cement was added, accounting for 1/9 of OPC, to promote the initial setting. The superplasticizer was utilized to reduce the water-to-cement ratio and to improve workability. Mixed-size polypropylene fibres with a mass ratio of 9 mm : 6 mm : 3 mm = 1 : 2 : 1 were chosen to establish a three-dimensional grid to lighten the floating of SAP beads.

The cellular concrete with a porosity of 25% was prepared in a forced mixer using the following procedure: (1) The superplasticizer was dissolved into mixing water. (2) The cement, fly ash, and silicon fume were blended for 2 min. (3) Water was added and blended until well combined. (4) Sat-SAP was added, and then, the fibres were scattered on the mixture until the SAP beads and fibres were evenly wrapped by mortar. (5) The mixture was poured into the moulds and compacted slightly to prevent SAP beads from floating up. The ordinary concrete was manufactured in the same machine using the conventional method. Based on GB/T 50081-2002 [19], three cubic samples with dimensions of 100 mm × 100 mm × 100 mm were taken for both concrete during the manufacturing process and cured for 28 days under the same condition. The ordinary concrete and the cellular concrete achieved the average compressive strength of 58.5 MPa and 62.1 MPa, respectively.

2.4. Specimen Preparation. Reinforcement structures and wooden moulds were fabricated on-site. The BFRP bars and steel bars were tied with a nylon ribbon and steel binding wire, respectively. The BFRP bars were equally sand-coated to progress the bond strength. After careful pouring and compacting, the specimens were covered with polyethylene sheets for 60-day curing. As a result of the inner cure effect of the SAP, additional water was not necessary, and no visible cracks were observed on the specimens.

Table 2: Mixture proportions (kg/m^3) of cellular concrete.

OPC	SAC	RS	SF	FA	W	PS	Sat-SAP	PP
769.6	85.5	761	213.8	17.1	188.1	17.1	137.8	1.46

Table 3: Mixture proportions (kg/m^3) of normal concrete.

OPC	RS	G	W	SF	PS
493	697	1025	125	48	0.5

According to GB/T 28900-2012 [20], three samples with a length of 500 mm were taken from both kinds of reinforcements for tensile tests. The BFRP was anchored in a ribbed steel tube with an epoxy resin to avoid slipping. The BFRP bars obtained different mechanical properties compared to the steel bars, as indicated by the tensile experiment. No postyield deformation was detected. The BFRP bars demonstrated a brittle failure and achieved an average ultimate strength of 870 MPa and an elastic modulus of 54 GPa. The HRB400-grade welded steel bar possessed a lower tensile strength of 562 MPa and a higher modulus of 185 GPa. Compared to the BFRP bars, the steel bars have evident plastic deformation, bestowing the distinctive behaviours from steel bar-reinforced specimens onto BFRP bar-reinforced specimens under static loads or explosions. All material parameters are tabulated in Table 4.

Table 4: Material parameters.

Reinforcement	Tensile strength (MPa)	Elastic modulus (GPa)
Steel bar	562	185
BFRP bar	870	54
Concrete	Compressive strength (MPa)	
Normal concrete	58.5	
Cellular concrete	62.1	

2.5. Experimental Setup. The shock tube, namely, the blast load simulator, is a mechanical device invented to produce dynamic air explosive loads with an overpressure, negative pressure, and impulse comparable to a typical blast event. The shock tube consists of a driver with a high-pressure vessel and a dual-membrane mechanism as a power source, followed by an expansion cone, a transition ring, and a dissipation ring. The specimen was mounted on an intact steel plate at the end of the main tube. The dissipation ring was isolated for an enclosed explosion simulation (Figure 3).

To attain a high-pressure dynamic air load, compressed air in the driver should burst in a flash. The driver (1 in Figure 3(a)) and the dual-membrane stage (2 in Figure 3(a)) were charged with compressed air simultaneously until the pressure in the dual-membrane stage is set to half of it in the driver. Subsequently, inflation or deflation of the dual-membrane stage induces the rupture of the membranes to stimulate the shock wave. Then, the reflected sparse waves from the driver overtake the shock wave, causing a declining overpressure where a negative pressure is also produced. The simulated blast shock wave is controlled by the inflation pressure. As exhibited in Figure 4, three working conditions with inflation pressures of 4.5 MPa, 5.5 MPa, and 6.5 MPa were developed in the experiment.

As shown in Figure 5, specimens were mounted in a steel box support by a chamfered steel block and covered with a steel plate. To prevent specimens from splitting away for the negative pressure, a fixed support was chosen. Fourteen M12 bolts were applied, resulting in a one-way condition with an effective area of 400 mm × 300 mm.

2.6. Measuring Methods. As shown in Figure 5(a), a few transducers and observation methods were applied to determine the comprehension dynamic response of the slabs. The failure properties were observed in detail.

2.6.1. Pressure History. Two pressure transducers (M102A02; PCB Piezotronics Inc, USA) were installed on the inner surface of the shock tube and the steel box, behind and in front of the slab, to record the overpressure history during the test and to compare the attenuation effect of the specimens.

2.6.2. Acceleration. A piezoelectric acceleration meter with a maximum range of 1000 g (K1001A; Kedong Electric Control System Co. Ltd., China) was also mounted on the bottom surface of the slab to record the acceleration history.

2.6.3. Deflection. An LVDT (linear variable differential transformer) displacement meter with a full range of 100 mm was installed in a steel tube aimed at the centre of the bottom surface of the specimens to record the displacement history (Figure 5(a)).

2.6.4. Cracks. The cracks were traced with a marker pen after shock wave exposure. The width of the main flexural crack was detected using a handheld microscope.

2.6.5. Strain. Investigating localized deformation of the slabs, strain gauges with a measuring range of 25000 $\mu\varepsilon$ were stuck on the rebars and concrete. The sizes were 5.5 mm × 3 mm and 55 mm × 5 mm, respectively. Bottom surface and reinforcement structure of a slab, respectively, have four strain gauges, disposed on a half and a quarter of their long side and short side (Figure 6). The positions for the rebar's gauges might not be accurate and consistent for different reinforcement configurations. The paste position of the steel and BFRP bars was polished until smoothened, pasted with strain gauges, and then encapsulated by cloth tape and epoxy to avoid damage in curing.

All transducers were inserted into a data acquisition instrument (WaveBook/512; IOtech, Inc., USA) and recorded continuously at a sampling frequency of 100 K.

3. Results and Discussion

3.1. Physical Observation and Cracks. Eleven slabs, except for BS1-3, were exposed to shock waves because BS1-2 had already been drastically damaged. After shock wave exposure, all steel bar-reinforced slabs and most specimens reinforced with BFRP bars could remain basically intact, demonstrating flexural failure, whereas BS1-2 suffered from punching shear failure. Because of the low reinforcement ratio and high overpressure load, the BFRP bars could not constrain the concrete and deform simultaneously. The incompatible deformation between the BFRP reinforcement structure and the concrete contributed to bucks of concrete debonding and being punched out, while the BFRP bars of BS1-2 were still undamaged and supported on the steel box with large deflections like arrows as a result of their long elastic deformation (Figure 7(a)). BS2-3 exhibited typical failure by brittle bending at the midspan with the BFRP bar ruptured in the concrete and pulled out at the clamp, while BS2-3 demonstrated evident residual deformation. As a result of improved reinforcement ratio, the coincident effect and constraint of the BFRP bar and concrete were also enhanced. Other specimens reinforced with BFRP bars though were damaged to varying degrees and also revealed plastic damage characteristics. Cracking, breach, and spalling were observed in some specimens. BS3-2 showed a large deformation without breakage and severe spall, indicating that a high reinforcement ratio could facilitate the plastic deformation of the concrete (Figure 8(c)). Some specimens embedded with BFRP bars (BS2-3, BS3-2, and BS3-3) also displayed spalling at both faces to different extents. BS1-1 had breaches at the midspan. On the contrary, SPs shared the

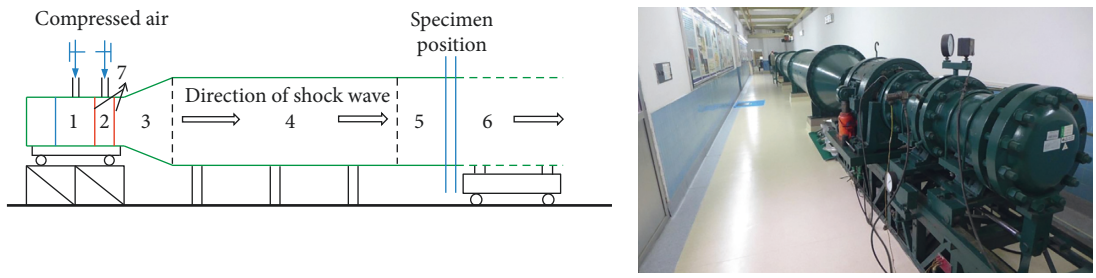

Figure 3: Shock tube device. (a) Schematic diagram of shock tube device: (1) high-pressure driver; (2) dual-membrane mechanism; (3) expansion cone; (4) transition ring; (5) target vessel; (6) dissipation ring; (7) aluminium membrane. (b) Real device.

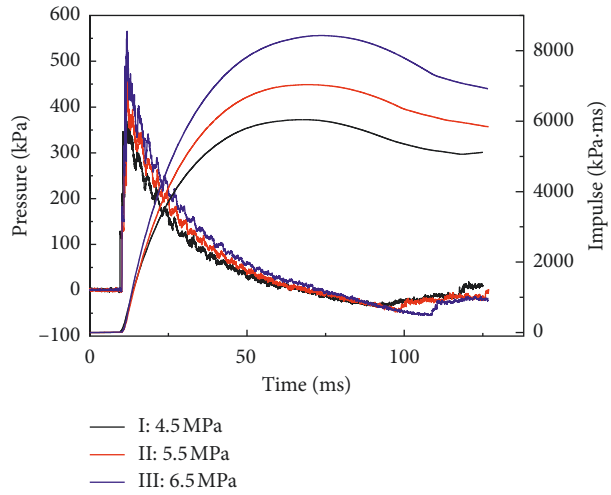

Figure 4: Incident overpressure and impulse histories of three working conditions.

same phenomenon in damage formation and cracking, except for different residual deformations. In general, with the same reinforcement ratio and loading regime, the specimens reinforced with BFRP bars showed more serious damage than the SPs. Herein, a higher reinforcement ratio could alleviate damage and produce behaviours similar to those of the SPs.

Most cracks were observed at the midspan and clamping positions on both sides of the slabs. As a result of negative pressure and free vibration, the front of the slabs would occasionally be in tension. Some specimens (BS2-2, BS3-2, and BS3-3) also exhibited cracks along the long side and formed crack webs, indicating a constrained condition of the four-side support. An increased reinforcement ratio could not evidently control the development of the crack. However, the SPs showed fewer cracks and smaller distributions, which might result from the relatively smaller displacement of SPs.

The measured widths of the flexural cracks are tabulated in Table 5. Both specimens reinforced with steel bars or BFRP bars shared the same phenomenon under identical working conditions, when having the same reinforcement ratio. The back and forth oscillations of the specimens resulted in cracks in the front face that were narrower than the cracks in the back face. A larger blast load induced grated cracks, while more reinforcement could mitigate cracking. However, the BFRP bar-reinforced slabs possessed more and notably finer cracks as a result of the anticracking ability provided by the polypropylene fibres added to the mortar matrix. The cracking of both specimens also illustrated that SPs absorbed the shock wave energy mainly through plastic deformation of steel rebars at the midspan, leading to local wider cracks, while the slabs with BFRP bars dissipated the energy through global vibration and concrete fracture, boiling down to a distinctive phenomenon.

3.2. Pressure Wave Characteristics. Typical pressure and impulse histories recorded by two sensors in front of and behind the specimens are presented in Figure 9. It was obvious that the cellular concrete reinforced with BFRP bars could sharply attenuate and oscillate the shock waves compared to the SPs. BS2-2 reduced 24.5% of the incident impulse through clipping its peak and reducing the slope of its rising edge. The other specimens reinforced with BFRP bars also exhibited impulse decline from 3.4% to 40.6%. It might be ascribed to the material properties and structural behaviours. The applied SAP endowed its porous structure, leading to a low-modulus concrete. The embedded BFRP bars with a low stiffness generated a more flexible structural

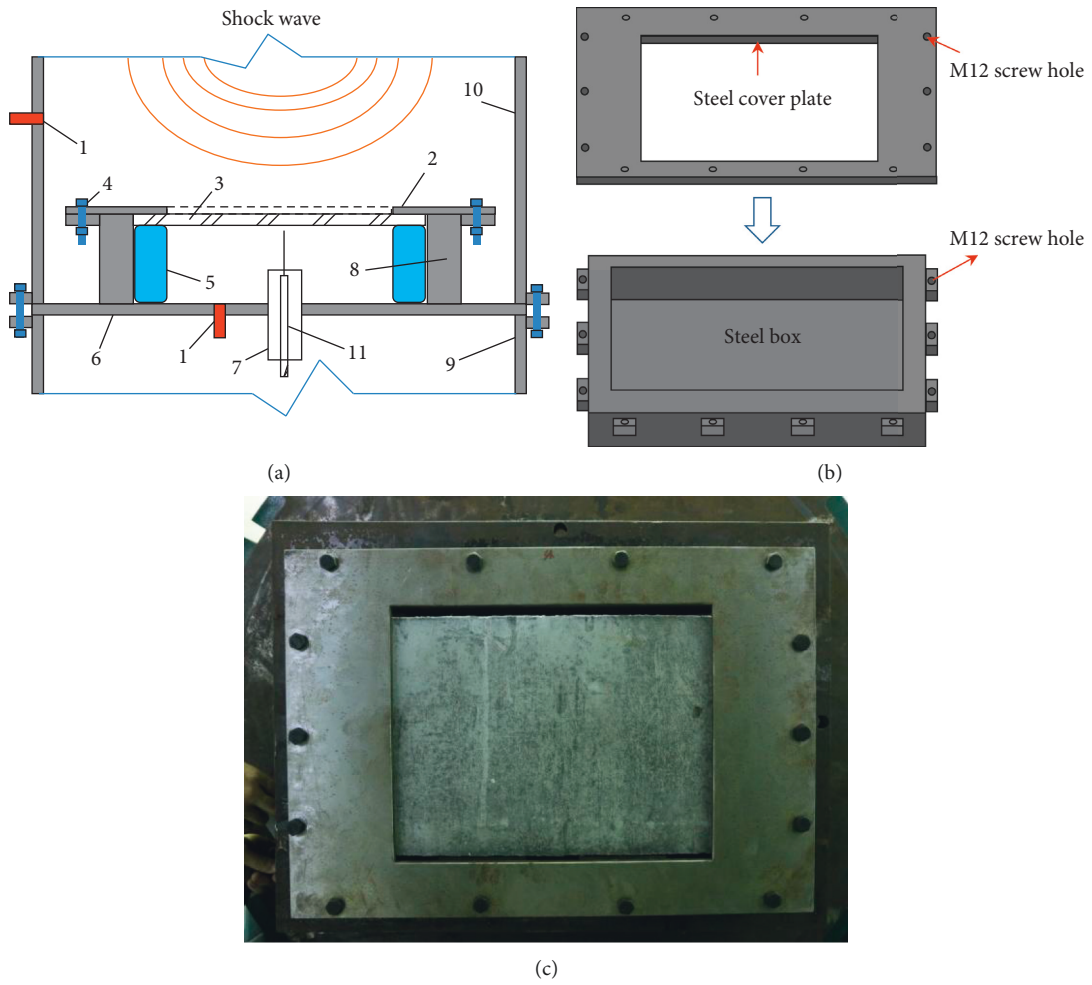

Figure 5: Setup in a shock tube. (a) Cross section of the target vessel: (1) pressure transducer; (2) steel cover plate; (3) specimen; (4) M12 bolt; (5) steel support; (6) steel plate; (7) steel tube; (8) steel box; (9) dissipation ring; (10) target vessel; (11) LVDT. (b) Fixation device. (c) Fixed specimen.

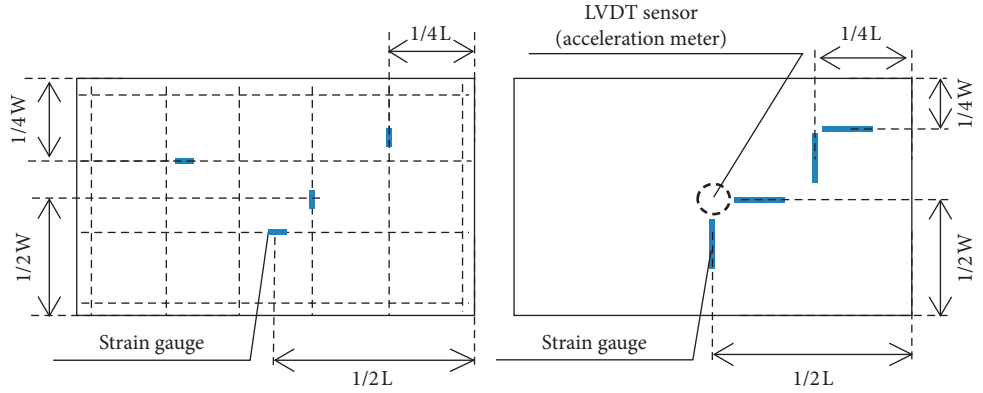

Figure 6: Measuring methods.

component compared to the SPs. Under blast loads, the BFRP bar-reinforced slabs achieved larger deformations and more intense vibrations, which could attenuate more energy than the SPs. The spatially distributed pores in the cellular concrete formed large free surfaces between the air and the mortar matrix. Stress waves were constantly reflected between the interfaces, resulting in conspicuous interfacial dispersion. As a whole, the porous structure itself acquired a low impedance and could diffract stress waves and absorb energy as constitutive dispersion [2]. Anticracking ability of

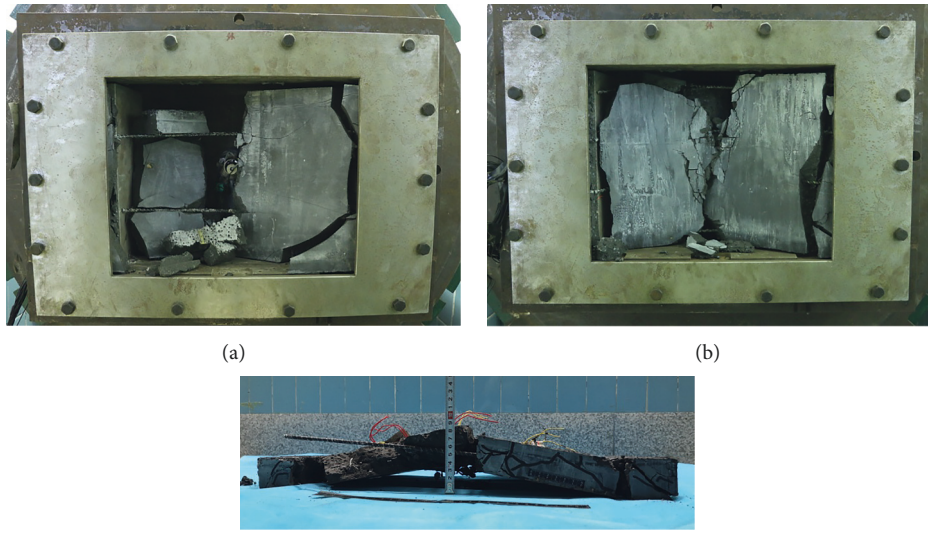

(a) (b)

(c)

Figure 7: Typical failure of specimens. (a) BS1-2. (b) BS2-3 (front view). (c) BS2-3 (side view).

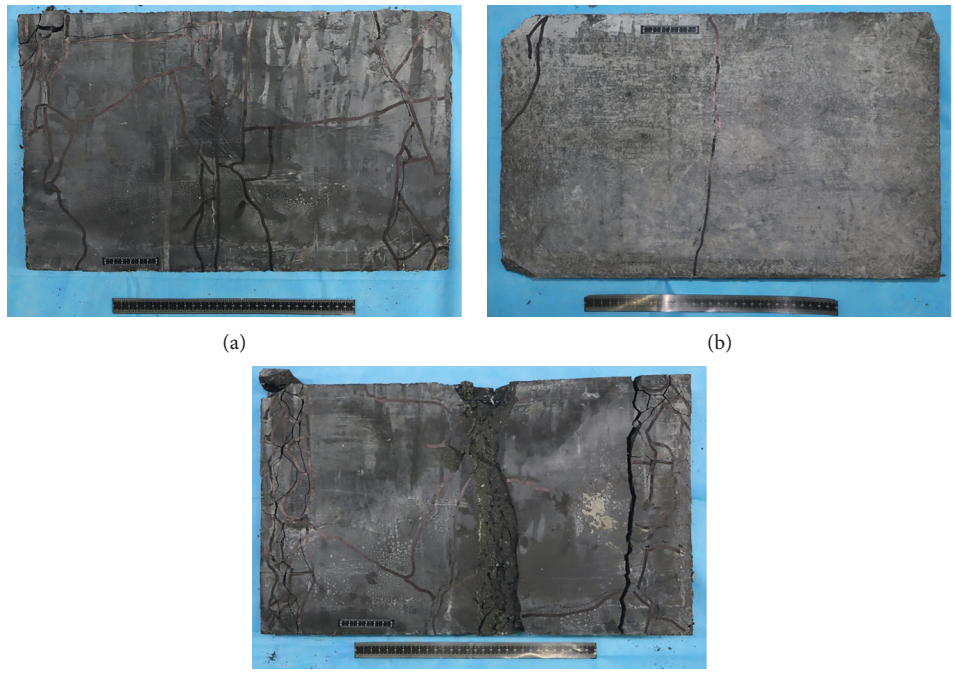

(a) (b)

(c)

Figure 8: Cracks. (a) BS2-2. (b) SP2-2. (c) BS3-2.

the cellular concrete might also hinder the transmission of shock waves.

3.3. Acceleration Measurement. Previous tests for steel-reinforced concrete slabs implied that the reinforcement was directly connected with acceleration. Heavier reinforcements induced higher accelerations compared to lightly reinforced slabs [21]. All valid data are summarized in Figure 10 and Table 6. It was illustrated that all acceleration histories accorded with the same law, while the lighter reinforcement led to a higher acceleration under identical loadings.

3.4. Deflections. The displacement histories could visually reflect the deformation ability and damage features of the specimens. Both kinds of slabs conformed with similar structural behaviours. Under shock wave loadings, specimens were forced to vibrate, which induced substantial

Table 5: Crack width of slabs.

ID	Crack width (mm)	
	Front surface	Back surface
SP2-1	0.05	1.05
SP2-2	0.1	1.4
SP2-3	0.25	1.85
BS1-1	2.5	0.95
BS1-2	—	—
BS2-1	0.1	0.15
BS2-2	0.25	0.35
BS2-3	—	—
BS3-1	0.05	0.1
BS3-2	0.25	0.35
BS3-3	0.35	0.35

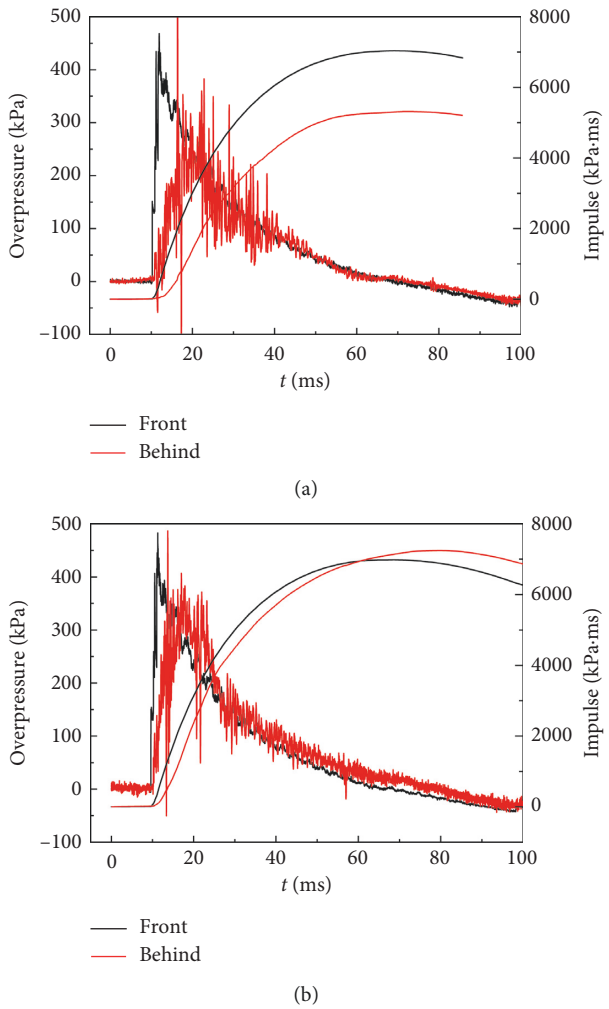

Figure 9: Typical overpressure and impulse history. (a) BS2-2. (b) SP2-2.

displacement and then returned back to the original site. Without the blast loading, the specimens freely vibrated with a smaller amplitude. In contrast, the reverse movement, which caused a negative displacement, was hardly visible in forced and free vibrations. Owing to the initial damage from

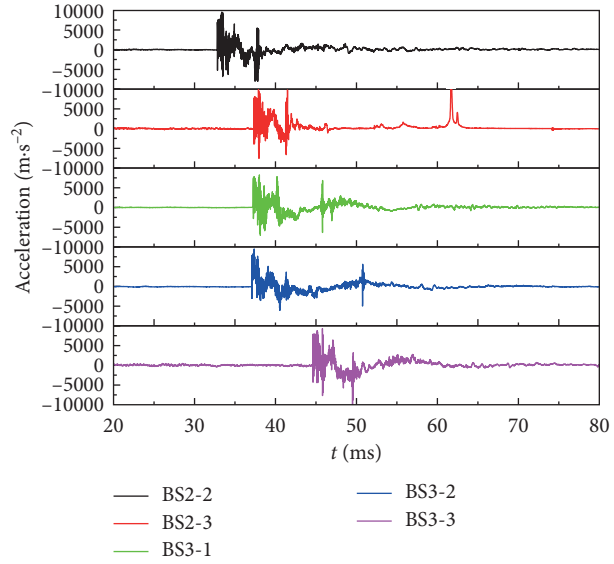

Figure 10: Acceleration-time histories.

Table 6: Acceleration-time history summary of slabs.

ID	Peak negative acceleration ($m \cdot s^{-2}$)	Peak positive acceleration ($m \cdot s^{-2}$)
BS2-2	−7992.93	9536.37
BS2-3	−7550.40	11880.07
BS3-1	−7061.91	8208.7
BS3-2	−6088.03	9481.63
BS3-3	−10715.25	9295.22

positive shock waves and lower negative pressures, the reverse movement had greater damping.

As shown in Figures 11(a) and 11(b), the displacement of the SPs increased with the improvement of the blast loading, mainly demonstrating no residual deformation. Compared to the SPs, the BFRP bar-reinforced slabs with the same reinforcement ratio exhibited markedly larger displacements in excess of the full-scale value of the LVDT. Different behaviours of BFRP bar-reinforced specimens might lie in the final stage of the deformation history. The shock wave load crippled the elastic property in the first stage, that is, the recovery capability of the specimens, elucidating various behaviours at the final stage. The cellular concrete slabs with BFRP bars deformed to the peak value at the first stage. However, concrete lacked elastic deformation than BFRP bars and cracked to failure, causing the specimen fail to recover. BS2-1 returned to the original position easily, while BS2-2 and BS2-3 developed more complex deformations, and BS2-3 failed with marked residual deflections at the first-stage movement. However, BFRP bars were still in the elastic stage in most cases, where the concrete properties determined the overall performance. Meanwhile, Figures 11(b) and 11(c) show that more reinforcement could partly diminish the deformation. The effect of increasing the reinforcement ratio might progress the curve characteristics, thus weakening the vibration. Heavier reinforcements strengthened the constraints of concrete and promoted integral stiffness and deformability. They also enhanced the

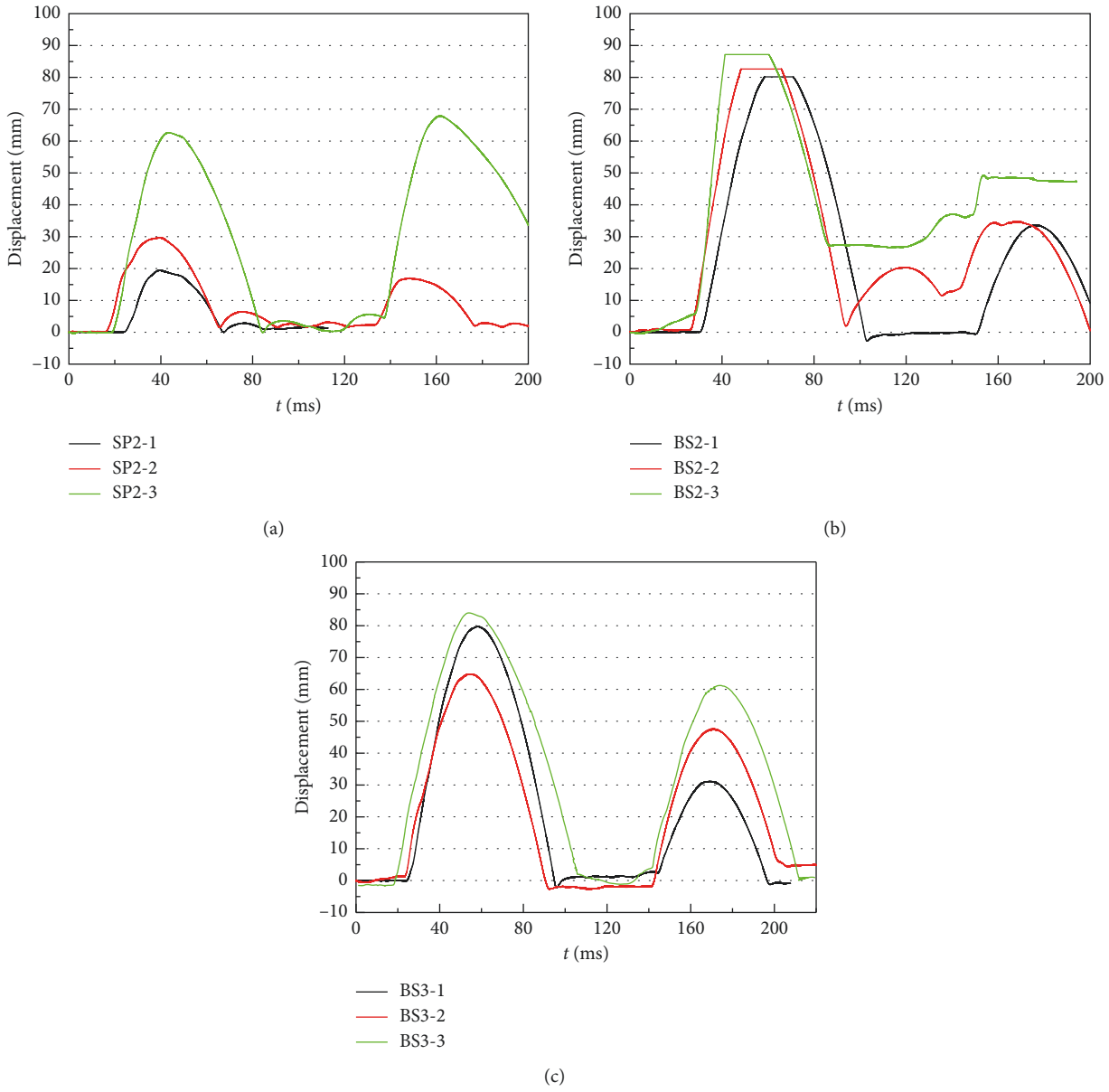

Figure 11: Time-displacement curves for slabs. (a) Time-displacement curve for SPs. (b) Time-displacement curve for BS2s. (c) Time-displacement curve for BS3s.

ductility of concrete, leading to behaviours similar to those of the SPs under the same blast loadings, as shown in Figure 11(a). However, the cellular concrete slabs reinforced with more BFRP bars still achieved larger deflections than the SPs. Reduced rigidity of the slab was also proved to improve blast resistance. On the contrary, large deformations could attenuate the wave-structure interaction and reduce the dynamic load [22].

3.5. Strains. Strain gauges were embedded in the reinforcements and stuck on the concrete to detect regional deformation. The four gauges were named CL, CW, QL, and QW according to the centre and quarter positions along the long/width side, which could also present behaviours of different parts of the specimens under shock waves. Because of the difficulties of dynamic measurements, data from some gauges were not recorded or reliable. Especially for concrete strains, the central gauges were damaged quickly with the serious and rapid cracking of the concrete. A few of the gauges at the corner were still unharmed as a result of the constraints of steel fixation.

Because of one-way support, the reinforcement strain gauge at the centre along the long side (BCL) was considered to be deformed the most, and the records of this gauge are shown in Figure 12. The strain history of all slabs varied according to a similar law that was consistent with the deformation behaviour. The oscillating curves elucidated flexible property of the BFRP bar-reinforced slabs and the process of interaction with the blast wave. The descending

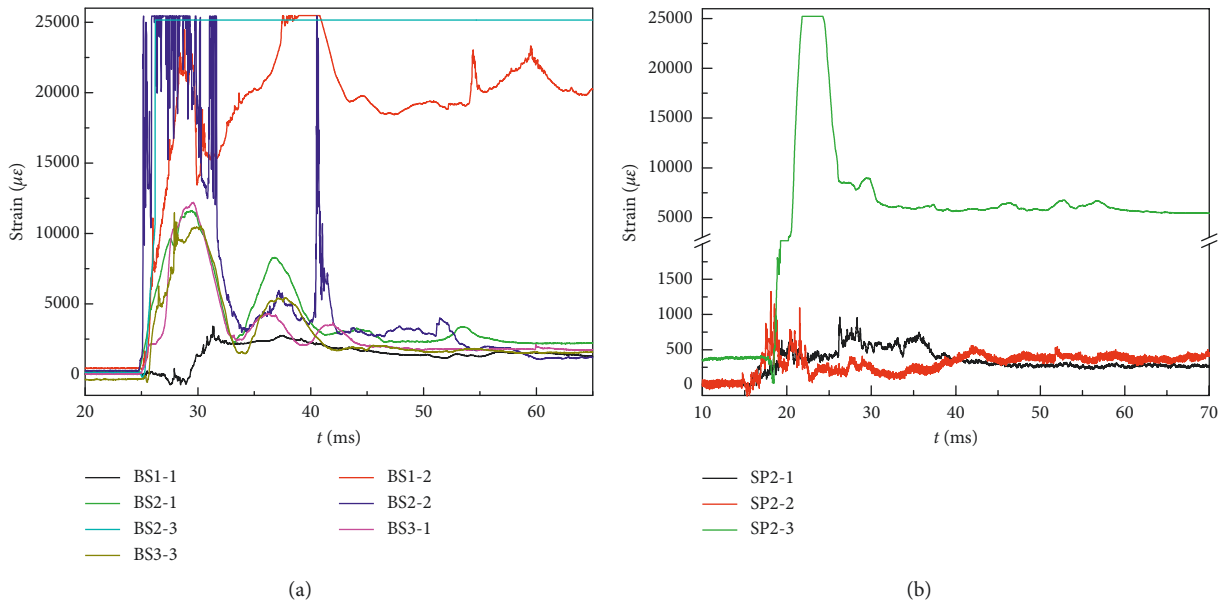

Figure 12: Strain history of the reinforcement (BCL). (a) BS specimens. (b) SP specimens.

strain and inconspicuous negative strain also resembled the deflection features, indicating the invisible reverse movement or arch of the specimens. Excluding severely damaged slabs BS1-2 and BS2-3, most of the other specimens could rebound to a low-strain status. Although the BFRP bars were always elastic before rupture, the concrete underwent plastic deformation and constrained the BFRP bars to an elastic but deformed condition. However, except for BS1-2, BS2-3, and BS1-2, the strain level of the other slabs was similar, indicating a weak relevance to the reinforcement ratio or shock wave loading. It also signified that the tensile strength of the BFRP was not sufficiently utilized, which was a common problem in FRP bar-reinforced concrete applications.

With regard to the SP specimens, although the macroscopic motion was coincident with that of the specimens reinforced with BFRP bars, the strain histories deviated notably. The strain curves of SPs fluctuated much less insignificantly because of the plastic property, but the peak and residual strain increased with enhanced loading.

The shock wave simulated by the shock tube device was actually a plane wave. Hence, there was no time difference for the strain distribution of the reinforcement structure. As noted above, slabs reinforced with BFRP bars demonstrated substantial displacement compared to the SPs, causing their different deformation in two directions. It is elucidated in Figure 13 that gauges CL and QL recorded different information, although the data from the same side agreed with a similar evolutionary law. Additionally, despite the fact that the BCL basically gained the largest peak strains, the other three gauges might not obtain the certain conclusion.

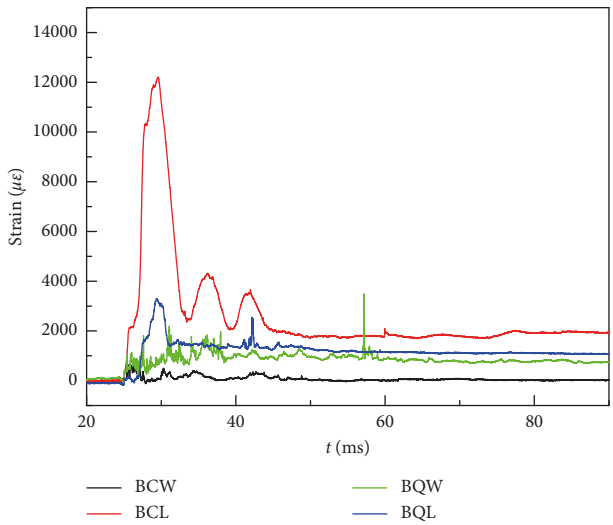

Figure 13: Reinforcement strain history of BS3-1.

4. Conclusion

The main purpose of this study is to investigate the blast resistance of BFRP bar-reinforced cellular concrete slabs (BSs) consisting of two novel materials. Using a shock tube device, eight BSs and three steel bar-reinforced normal concrete slabs (SPs) were tested under simulated blast loadings. Based on the results and discussions presented, the following conclusions can be drawn:

(1) The cellular concrete and BFRP bar have a low stiffness, making BSs more flexible and resulting in different behaviours from SPs under explosive loads. BSs acquire a distinctive method to dissipate shock wave energy through more intensive vibrations, larger deflections, and more severe cracking, which are also observed in the strain history of BFRP bars.

(2) The severe vibrations of BSs, indicating a strong wave-structure interaction, actually attenuate the dynamic loading. In addition to the porous structure of cellular concrete, the interfacial constitutive

dispersion causes the BSs to obtain a reasonable energy-absorbing ability and smaller crack width.

(3) BFRP bars have a higher strength and are employed in the elastic state. Despite the fact that BSs acquired some undesirable features in the experiment, such as greater deformation and cracks, it can be mitigated by improving the reinforcement ratio. The ductile failure mode can be achieved in the BFRP-reinforced specimens by using a rational design method. The material properties can provide BSs with an excellent antiblast ability that is even better than that of the SPs in the current study.

Data Availability

The data used to support the findings of this study are available from the corresponding author upon request.

Conflicts of Interest

The authors declare that there are no conflicts of interest regarding the publication of this paper.

Acknowledgments

This work was supported by the National Key Research and Development Program of China (2016YFB0303501-04).

References

[1] Z. Deng, H. Cheng, Z. Wang, G. Zhu, and H. Zhong, "Compressive behavior of the cellular concrete utilizing millimeter-size spherical saturated SAP under high strain-rate loading," *Construction and Building Materials*, vol. 119, pp. 96–106, 2016.

[2] F. Wang, J. Yang, S. Hu, X. Li, and H. Cheng, "Influence of superabsorbent polymers on the surrounding cement paste," *Cement and Concrete Research*, vol. 81, pp. 112–121, 2016.

[3] H. Cheng, Z.-J. Cheng, X.-C. Pan, and Z.-M. Hou, "Super-absorbent polymer concrete and its preparation method," Chinese Patent ZL201210345029.4, 2014, in Chinese.

[4] J. W. Tedesco and D. W. Landis, "Wave propagation through layered systems," *Computers & Structures*, vol. 32, no. 3-4, pp. 625–638, 1989.

[5] G. C. Hoff, "Shock-absorbing materials, report 2: cellular concrete as a backpacking material," 6-763, Technical Report Archive & Image Library, Vicksburg, MS, USA, U.S. Army Engineer Waterways Experiment Stations, 1971.

[6] J. Ren, Z. Deng, H. Cheng, L. Zhou, and X. Zheng, "Numerical simulation of dynamic mechanical properties of porous concrete fabricated with the SAP," *Modelling, Measurement and Control B*, vol. 86, no. 2, pp. 535–556, 2017.

[7] A. Patnaik, "Applications of basalt fiber reinforced polymer (BFRP) reinforcement for transportation infrastructure," in *Proceedings of the Developing a Research Agenda for Transportation Infrastructure Preservation and Renewal Conference*, pp. 175–184, Washington DC, USA, November 2009.

[8] Z. Sun, Y. Yang, W. Yan, G. Wu, X. He, and X.-Y. He, "Moment-curvature behaviors of concrete beams singly reinforced by steel-FRP composite bars," *Advances in Civil Engineering*, vol. 2017, Article ID 1309629, 14 pages, 2017.

[9] G. Zhu, H. Cheng, and Z. Deng, "Experimental study on the bond behavior between SAP concrete and BFRP bars," *International Journal of Earth Sciences and Engineering*, vol. 8, p. 7, 2015.

[10] G.-X. Zheng, H. Cheng, and G.-H. Zhu, "Analysis and experimental research on flexural capacity of SAP concrete beam reinforced with FRP," *Journal of Logistical Engineering University*, vol. 33, pp. 6–10, 2017, in Chinese.

[11] J.-R. Gu and Z.-G. Wang, "Axial compression of SAP concrete columns with carbon hybrid fiber-glass reinfbrced plastic tendon," *Journal of Ordnace Equipment Engineering*, vol. 39, pp. 177–182, 2018, in Chinese.

[12] K. Zieliński and P. Olszewski, "The impact of basaltic fibre on selected physical and mechanical properties of cement mortar," *Concrete Precasting Plant and Technology*, vol. 71, pp. 28–33, 2005.

[13] M. E. M. Mahroug, A. F. Ashour, and D. Lam, "Experimental response and code modelling of continuous concrete slabs reinforced with BFRP bars," *Composite Structures*, vol. 107, pp. 664–674, 2014.

[14] M. Hassan, B. Benmokrane, A. Elsafty, and A. Fam, "Bond durability of basalt-fiber-reinforced-polymer (BFRP) bars embedded in concrete in aggressive environments," *Composites Part B: Engineering*, vol. 106, pp. 262–272, 2016.

[15] F. Elgabbas, P. Vincent, E. A. Ahmed, and B. Benmokrane, "Experimental testing of basalt-fiber-reinforced polymer bars in concrete beams," *Composites Part B: Engineering*, vol. 91, pp. 205–218, 2016.

[16] X. Fan and M. Zhang, "Behaviour of inorganic polymer concrete columns reinforced with basalt FRP bars under eccentric compression: an experimental study," *Composites Part B: Engineering*, vol. 104, pp. 44–56, 2016.

[17] J. Feng, Y. Zhou, P. Wang et al., "Experimental research on blast-resistance of one-way concrete slabs reinforced by BFRP bars under close-in explosion," *Engineering Structures*, vol. 150, pp. 550–561, 2017.

[18] ACI Committee, *Guide for the design and construction of structural concrete reinforced with fiber-reinforced polymer (FRP) bars*, ACI Committee, Farmington Hills, MI, USA, 2015.

[19] China Standard, *GB/T, 50081-2002 Method for Testing Mechanical Properties of Normal Concrete*, China Standard, Beijing, China, 2002.

[20] ISO, *EN. 15630-1: 2010. Steel for the Reinforcement and Prestressing of Concrete–Test Methods–Part 1*, ISO, Geneva, Switzerland, 2010.

[21] M. Zineddin and T. Krauthammer, "Dynamic response and behavior of reinforced concrete slabs under impact loading," *International Journal of Impact Engineering*, vol. 34, no. 9, pp. 1517–1534, 2007.

[22] H. Y. Low and H. Hao, "Reliability analysis of direct shear and flexural failure modes of RC slabs under explosive loading," *Engineering Structures*, vol. 24, no. 2, pp. 189–198, 2002.